2010

Interface polarization coupling in piezoelectric-semiconductor ferroelectric heterostructures

Venkata M. Voora
University of Nebraska-Lincoln

Tino Hofmann
University of Nebraska-Lincoln, thofmann4@unl.edu

M. Brandt
Institut für Experimentelle Physik II, Universität Leipzig, 04103 Leipzig, Germany

M. Lorenz
Institut für Experimentelle Physik II, Universität Leipzig, 04103 Leipzig, Germany

M. Grundmann
Institut für Experimentelle Physik II, Universität Leipzig, 04103 Leipzig, Germany

See next page for additional authors

Interface polarization coupling in piezoelectric-semiconductor ferroelectric heterostructures

Venkata M. Voora,[1] T. Hofmann,[1] M. Brandt,[2] M. Lorenz,[2] M. Grundmann,[2] N. Ashkenov,[2] H. Schmidt,[3] N. Ianno,[1] and M. Schubert[1]

[1]*Department of Electrical Engineering and Nebraska Center for Materials and Nanoscience, University of Nebraska–Lincoln, Lincoln, Nebraska 68588, USA*

[2]*Institut für Experimentelle Physik II, Universität Leipzig, 04103 Leipzig, Germany*

[3]*Institut für Ionenstrahlphysik und Materialforschung, Forschungszentrum Dresden-Rossendorf e.V., 01328 Dresden, Germany*

(Received 18 November 2009; revised manuscript received 28 March 2010; published 5 May 2010)

We present a dielectric continuum model approach for studying the electrical polarization properties of interface polarization coupled $BaTiO_3$, $BaTiO_3$-ZnO, and ZnO-$BaTiO_3$-ZnO thin-film structures consisting of several hundred nanometer thick layers. Our model augments the effects of electric field driven switchable polarization and depletion layer formation with spontaneous interface polarization coupling. Wurtzite-structure (piezoelectric) *n*-type ZnO and perovskite-structure (ferroelectric) highly insulating $BaTiO_3$ layers were prepared and investigated. The coupling between the nonswitchable spontaneous polarization of ZnO and the electrically switchable spontaneous polarization of $BaTiO_3$ causes strong asymmetric polarization hysteresis behavior. The *n*-type ZnO reveals hysteresis-dependent capacitance variations upon formation of depletion layers at the ZnO/BTO interfaces. We obtain a very good agreement between our model generated data and our experiment. Our model approach allows for derivation of the amount and orientation of the spontaneous polarization of the piezoelectric constituents and can be generalized toward multiple-layer piezoelectric-semiconductor ferroelectric heterostructures. We identify interface polarization coupled triple-layer ZnO-BTO-ZnO heterostructures as two-terminal unipolar ferroelectric Bi-junction transistor for use in memory storage.

DOI: 10.1103/PhysRevB.81.195307 PACS number(s): 77.80.Fm, 77.80.Dj, 73.40.Qv, 81.05.Dz

I. INTRODUCTION

The physics and device characteristics of metal-ferroelectric-metal (MFM), ferroelectric-semiconductor (FS), metal-ferroelectric-semiconductor (MFS), and semiconductor-ferroelectric-semiconductor (SFS) heterostructures continue to attract attention due to their large potential for electronic and optoelectronic device applications.[1–11] The ferroelectric constituent possesses switchable dielectric polarization. This polarization can be exploited for modification of the electronic and optical properties of a semiconductor heterostructure. Hysteresis properties of the ferroelectric polarization allows for bistable interface polarization configuration and potentially for bistable heterostructure operation modes. In this paper, we discuss the incorporation of piezoelectric semiconductors with spontaneous polarization in combination with ferroelectric materials. We anticipate coupling phenomena between the spontaneous polarizations at their common interface.[12] Such configurations are of interest for bistable history-dependent heterostructure operation modes, such as for low-energy consumptive nonvolatile memory devices or ferroelectric field-effect transistors.[13,14] MFS heterostructures typically reveal voltage-asymmetric polarization response.[15–22] Xu *et al.*[15] suggested a model based on energy-band theory to explain the asymmetric behavior observed in lead zirconate titanate, barium titanate, strontium niobate, and lead barium niobate thin films deposited on silicon. Wurfel *et al.*[17,18] and Batra *et al.*[19] considered ferroelectric depolarization and interface depletion layer formation for MFS and SFS structures, where depolarization charges are responsible for the decay of the ferroelectric polarization, and depletion formation occurs due to the band bending at the semiconductor-ferroelectric interface. Berman solved the Poisson equation for MFS structures in analogy to MFM structures with symmetric ferroelectric hysteresis properties and bound interface charges and successfully described the observed asymmetric hysteresis properties.[16,20]

As discussed in this work, for materials with appropriate electronic configurations, the net component of the interface charge is associated with internal electric fields, which can be used to modify or create space charge regions on either side of the interface. The semiconductor and the piezoelectric constituent may be comprised within the same material. Such heterostructures can be composed of, for example, from piezoelectric semiconducting wurtzite-structure ZnO and ferroelectric highly insulating perovskite-structure $BaTiO_3$ (BTO). Solid-state materials with lack of symmetry inversion possess piezoelectric (stress- or strain-induced) polarization. Wurtzite-structure materials exhibit in addition to stress- or strain-induced polarization a spontaneous polarization component, which arises from the molecular arrangement within the unit cell. In equilibrium condition, a permanent static electric dipole forms along the lattice *c* axis, with orientation and magnitude depending on the elemental lattice constituents.[23–25] The amount of the spontaneous polarization depends on the elemental constitution within the wurtzite lattice and can be changed, for example, by alloying.[26,27] The interface polarization coupling in piezoelectric-semiconductor ferroelectric heterostructures produces voltage-asymmetric hysteresis-dependent internal electric field variations, which affect their capacitance properties. In this paper, we introduce *n*-type conductive ZnO as the piezoelectric semiconducting constituent. The approach lined out is sufficiently general and also allows for incorporation of *p*-type conductive materials, as well as other piezoelectric semiconductors than ZnO. BTO is incorporated as the ferro-

electric constituent. We present a dielectric continuum model approach. We employ this approach for predicting and discussing the electrical polarization properties of interface polarization coupled $BaTiO_3$, $BaTiO_3$-ZnO, and ZnO-$BaTiO_3$-ZnO thin-film heterostructures. We augment known ferroelectric polarization model approaches with the phenomenon of electric-field and polarization-induced depletion layer formation. We predict and observe experimentally strong asymmetric polarization hysteresis behavior due to the *n*-type conductivity in ZnO, which produces ferroelectric hysteresis-dependent electrical capacitance variations upon formation of depletion zones at the ZnO-BTO interfaces. We obtain a very good quantitative agreement between our model generated data and our experiment. Our model approach allows for derivation of the amount and orientation of the spontaneous polarization of the piezoelectric constituent and can be generalized toward multiple-layer piezoelectric-semiconductor ferroelectric heterostructures. A qualitative interpretation based on our model is further used to explain observed electrical conductance hysteresis in $BaTiO_3$-ZnO and ZnO-$BaTiO_3$-ZnO thin-film heterostructures, with potential for use in memory storage applications, and ferroelectric field-effect transistors.[13,14] We note that the typical layer thickness considered here is on the order of fractions of micrometers or few micrometers, where our dielectric continuum model is reasonably applicable. Strong contemporary interest exists both theoretical and experimental on monolayer or few-layer ferroelectric heterostructures, see, for example, Ref. 28. At the nanoscale, additional phenomena will occur, and the here presented model does not apply to "genuinely thin," i.e., few atomic layer structures instantly. We further note that mechanical constraints imposed by the substrate or by the lattice mismatch between heterostructure constituents are very important and may need to be considered since strain imposed during pseudomorphic or partially relaxed heteroepitaxial growth will add another interface polarization component. This piezoelectric polarization can easily be augmented as new variable within our model approach which needs to be added to the spontaneous polarization component with magnitude and direction depending on type and amount of built-in strain for each layer.

Knowledge of magnitude and orientation of the spontaneous polarization is not exhaustive for many piezoelectric materials with spontaneous electric lattice dipole. Even for materials with large spontaneous polarization, such as ZnO, little knowledge has been gathered so far. Theoretical investigations have calculated the charge per atom and the lattice parameters of the material, resulting in values for the spontaneous polarization of $P_{ZnO}=-0.032$ C/m^2,[23] $P_{ZnO}=-0.05$ C/m^2,[24] and $P_{ZnO}=-0.057$ C/m^2.[25] The spread of the values obtained is larger in other studies, which rely on experimental values for the lattice constants.[29,30] Initial experimental studies employing second harmonic generation reported $P_{ZnO}=-0.07\pm0.015$ C/m^2.[31] The influence of the ZnO polarization on the electronic structure and the formation of defects has been studied by photoluminescence spectroscopy, current-voltage, capacitance-voltage, and Hall-effect investigations.[32–37] The two different polar surfaces of ZnO (Zn or O termination) have been investigated for their physical properties. The relative intensities of near-band-gap photoluminescence features were found different between the two polar surfaces, which was attributed to different surface Fermi-energy positions.[34] It was reported that free charge carrier densities[33,35–37] and surface chemistry mechanisms differ[32] and a remarkable difference in the electronic work function was observed.[33] Different surface reconstructions were reported recently.[38] The polarity of a ZnO single crystal can be determined by etching a polar surface.[39] The polarity was also studied in high-quality crystalline ZnO thin films by dispersion x-ray diffraction,[40–42] scanning nonlinear dielectric microscopy,[43] angular resolved x-ray photoelectron diffraction,[44,45] and coaxial-impact collision-ion scattering spectroscopy.[46–48] Detailed studies of the spontaneous polarization properties have been carried out in the structurally equivalent AlGaN-GaN material system.[26,27] At heterostructure interfaces within the AlGaN system, in addition to the spontaneous polarization component a large compressive or tensile strain-induced polarization exists. The dependence of both polarizations on the Al concentration, for example, in AlGaN-GaN, can be studied by investigating the electronic properties of two-dimensional carrier gases, which can form at the interface. Similar investigations have been carried out in the MgZnO-ZnO system[49–51] where, however, the lattice-mismatch induced strain is smaller than in the AlGaN-GaN system, and a cubic (rocksalt-structure) phase transition occurs in $Zn_xMg_{1-x}O$ for $x\approx0.65$.[52] Experimental polarization values have been obtained by numerical evaluation of the photoluminescence shift in MgZnO-ZnO quantum well structures. The polarization-induced electric field within the quantum wells affects the optoelectronic properties by band bending and field-induced emission wavelength shift (Stark-effect).[53] The obtained values represent the net polarization of the heterostructure constituents, both possessing piezoelectric and spontaneous polarization, and were found to vary widely among different samples and also from theoretical predictions.[23] The decomposition of the net polarization into strain-induced and piezoelectric components requires knowledge of lattice constants and piezoelectric coefficients.

We have recently reported on electro-optic and electric investigations of ZnO-BTO heterostructures,[12,54–59] where we observed asymmetric polarization properties. Our model approach was briefly mentioned in two previous proceedings publications.[57,60] In this work, we present our model approach in detail and give a quantitative comparison with experimental data. Section II details the model approach. Section III discusses experimental procedures and sample details. Section IV presents results and discussions. Conclusions are summarized in Sec. V. Appendix A recalls the phenomenological ferroelectric polarization approximation employed here. Appendix B describes the experimental polarization measurement technique (Sawyer-Tower circuit), and the employed numerical iteration procedure is outlined in Appendix C.

II. THEORY

Figure 1 depicts a schematic presentation of a piezoelectric semiconductor (P)–ferroelectric (F)–piezoelectric semi-

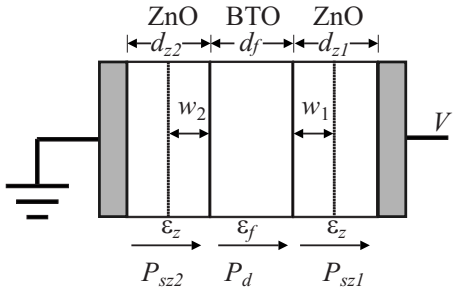

FIG. 1. Schematic of a piezoelectric semiconductor (P)-ferroelectric (F)-piezoelectric semiconductor (P) heterostructure (PFP) with spontaneous piezoelectric and ferroelectric polarization P_{sz} and P_d, respectively, embedded between ideal contacts. Components for P and F are here represented by ZnO and $BaTiO_3$ (BTO), respectively, with symmetric layer sequence. The left interface of the left layer is connected to ground, the right interface of the right layer is at potential V. Depletion layer formation occurs at interfaces (from left to right) P-F (w_2) and/or F-P (w_1) for n-type (conductive) constituents P and insulating (barrier) F. w_1, w_2 depend on V, sample properties (P_{sz1}, P_{sz2}, layer thickness d_{z1}, d_{z2}, d_f, dielectric constants ε_z, ε_f), and sample history (P_d).

conductor (P) heterostructure (PFP) embedded between ideal contacts. The biased and grounded P layers (ZnO) have layer thickness d_{z1} and d_{z2}, respectively, and layer F (BTO) has thickness d_f. Layer F is considered ideally as an insulator but more realistically here as a highly resistive dielectric layer and which acts as an electronic barrier. Layers P are treated as n-type semiconductors with equal net dopant concentration N_{c1} (biased layer P) and N_{c2} (grounded layer P). The nonswitchable spontaneous polarization in layers P causes a permanent electric field and biases the switching behavior of the ferroelectric polarization in layer F. Both polarizations influence the formation of space charge regions, such as depletion or accumulation layers within layer P toward its interface with layer F. Two possible polar (crystallographic) orientations for P give rise to two possible spontaneous polarization vector orientations P_{sz}. In triple or multiple layer heterostructures, polarization coupling can occur at multiple interfaces[61–67] and will become interdependent. The charge distribution at the interfaces will affect the electrical properties of the overall heterostructure. For the triple layer structure, two scenarios can be envisioned, where either layer F is embedded by layers P or vice versa. In this section, we present a model describing a PFP heterostructure. The model equations for the situation FPF are obtained in straightforward manner using the scheme discussed below.

In a PFP heterostructure, at each of the P-F and F-P interfaces, depletion or accumulation layers can be formed toward each interface within each layer P, depending on P and F materials' properties, history, and external bias. Upon depletion layer formation, a capacitive sublayer is formed in layer P toward layer F, which augments a series capacitance in addition to layer F. Assuming homogeneous distribution of net donor density N_c within layer P of thickness d, a charge depletion layer with thickness w causes a potential step

$$V_{\text{depletion}} = \frac{eN_c}{\varepsilon}\int_0^{w\le d} x dx, \tag{1}$$

where ε is the dielectric constant in P, e is the electronic unit charge, and integration occurs along spatial variable x parallel to the electric field. The sources of the electric field within the depletion layer are the ionized immobile donors, which may be partially screened by the net polarization charge at the P-F interface. The remaining nondepleted sublayer $d-w$ of P is here considered ideally conductive, i.e., with negligible series resistance (flatband situation). Accordingly, accumulation layer formation is omitted since no potential drop can occur across any nondepleted part of layer P. The path integral over the internal electric field between the two electrodes in Fig. 1 delivers

$$V = d_f E_f + \int_0^{w_1} E_{z1} dx + \int_0^{w_2} E_{z2} dx, \tag{2}$$

which depends on the electric field across layer F, E_f. E_{z1} and E_{z2} are the fields in layers P to the right and left of layer F, respectively. E_f can be expressed by P_d, D_f, and ε_f, the spontaneous (ferroelectric) polarization, displacement, and dielectric constant of layer F, respectively,

$$E_f = \varepsilon_f^{-1}(D_f - P_d). \tag{3}$$

Note that P_d is a function of E_f. With $D_f = \sigma_b$, the surface charge at the bottom of layer F, and Eq. (1), we obtain

$$V = \frac{d_f}{\varepsilon_f}(\sigma_b - P_d) + \frac{1}{2}\left(\frac{eN_{c1}}{\varepsilon_z}w_1^2 - \frac{eN_{c2}}{\varepsilon_z}w_2^2\right). \tag{4}$$

For nonzero E_{z2}, it must point from right to left in Fig. 1 in order to form depletion, which results in negative potential due to layer w_2 in Eq. (4). Dielectric displacement continuity requirement (from left to right in Fig. 1) across interface P-F results in

$$eN_{c1}w_1 + P_{sz1} = E_f\varepsilon_f + P_d, \tag{5}$$

and across F-P

$$E_f\varepsilon_f + P_d = -eN_{c2}w_2 + P_{sz2}. \tag{6}$$

P_{sz1} and P_{sz2} are the spontaneous (piezoelectric) polarizations of layers P and ε_z is the dielectric constant of layers P. Equations (4)–(6) connect quantities σ_b, E_f, w_1, and w_2. Note that we assume no spontaneous interface charge at the depleted–nondepleted interface within layer P, consistent with the above made "flatband" assumption.

Variation in orientation and magnitude of polarization in layers P results in varieties of possible arrangements. For example, assuming for simplicity $|P_{sz1}| = |P_{sz2}|$, one can have $P_{sz1} = P_{sz2} = P_{sz}$, i.e., P^+FP^+, or $P_{sz1} = -P_{sz2} = P_{sz}$, i.e., P^+FP^-, or P^-FP^+, or P^-FP^-, accordingly. Depending on external bias V and material parameter situations, different configurations of depletion layer formation can occur (Table I). Neither w_1 and w_2 can be negative or larger than d_{z1} and d_{z2}. Scheme (A) is the nondepleted state of both layers P. Scheme (B) is when the biased layer P (right in Fig. 1) possesses a finite depletion layer ($0 < w_1 < d_{z1}$), and the grounded layer P (left in Fig. 1) is nondepleted. Scheme (C) is when grounded

TABLE I. Configuration schemes according to depletion layer formation, variables w_1, w_2 in Eq. (10), and corresponding junction (Jctn) conditions (forwardlike "F," reverselike "R;" see Sec. IV B for definition of F and R) between piezoelectric and ferroelectric (P-F), and ferroelectric and piezoelectric (F-P) constituents of the PFP heterostructure shown in Fig. 1.

Scheme	w_1	w_2	Jctn P-F	Jctn F-P
(A)	0	0	F	F
(B)	$0<w_1<d_{z1}$	0	R	F
(C)	0	$0<w_2<d_{z2}$	F	R
(D)	$0<w_1<d_{z1}$	$0<w_2<d_{z2}$	R	R
(E)	d_{z1}	0	R	F
(F)	0	d_{z2}	F	R
(G)	$0<w_1<d_{z1}$	d_{z2}	R	R
(H)	d_{z1}	$0<w_2<d_{z2}$	R	R
(I)	d_{z1}	d_{z2}	R	R

layer P possesses a finite depletion layer ($0<w_2<d_{z2}$), and biased layer P is nondepleted. In scheme (D) both biased and grounded layers P are partially depleted ($0<w_1<d_{z1}$, $0<w_2<d_{z2}$). In scheme (E) the biased and grounded layers P are fully and nondepleted, i.e., $w_1=d_{z1}$, $w_2=0$, respectively. Scheme (F) is the reverse case of (E), i.e., $w_1=0$, $w_2=d_{z2}$. Further conceivable schemes are (G) and (H) similar to (B) and (C), except with $w_2=d_{z2}$ and $w_1=d_{z1}$, respectively, and scheme (I) with $w_1=d_{z1}$, $w_2=d_{z2}$. Note that for schemes (E)–(I), the space-charge related displacement terms $eN_{c1}d_z$ and/or $-eN_{c2}d_z$ are constant, and additional potential E_zd_z and displacement $E_z\varepsilon_z$ terms must be added to the appropriate sides of Eqs. (4)–(6), respectively.

In our model approach we aim at comparison with experimentally observable time-dependent electric potential variations, i.e., Sawyer-Tower (ST) measurements (Appendix B). ST measurements monitor $d/dt(V)=d/dt(V_{in}-V_o-V_{bi})$ across our heterostructure relative to a normal (standard) capacitor structure, where V_{in} is the applied bias to the series of sample and normal capacitor, V_o is the potential drop across the normal capacitor, and V_{bi} is the effective built-in potential (sum of all conduction band offsets) across the sample. The ohmic series resistance R_s of the sample between ground and bias contact causes parasitic current. R_s is dominated by the highly resistive layer F. R_s is measured by experiment and considered here as a constant. ST measurements are commonly employed for dielectric hysteresis measurements of ferroelectric capacitor structures. We are here interested in calculation of time derivatives of the charge leaving or entering ground. Because all layers are in series and for continuous time-harmonic excitation dV/dt, in steady-state condition the charge variation at the ground contact equals $d\sigma_b/dt$. Taking the time derivative of Eqs. (4)–(6) and substituting differentials

$$dP_d = \left(\frac{dP_d}{dt}\right)\left(\frac{dE_f}{dt}\right)^{-1} dE_f, \tag{7}$$

we obtain linear relations between dE_f/dt and $d\sigma_b/dt$, with the time derivative of the external potential

$$\frac{dE_f}{dt} = \gamma\frac{dV}{dt} \tag{8}$$

and

$$\frac{d\sigma_b}{dt} = \gamma\left(\varepsilon_f + \frac{dP_d}{dE_f}\right)\frac{dV}{dt}, \tag{9}$$

with

$$\gamma = \left(d_f + \frac{w_1+w_2}{\varepsilon_z}\left[\varepsilon_f + \frac{dP_d}{dE_f}\right]\right)^{-1}. \tag{10}$$

The coefficient γ differs for the different schemes by the values of the depletion layer variables w_1 and w_2 (Table I). Without hysteresis in $\frac{dP_d}{dE_f}$, Eqs. (8) and (9) become simple linear relationships.

The ferroelectric nature of layer F causes nonlinear dependence $P_d(E_f)$, which renders the ferroelectric hysteresis. $P_d(E_f)$ is an intricate function of microstructure, defects, and time. The hyperbolic tangent function[2] is used here as approximation for the saturation polarization P_{sat} of layer F

$$P_{sat}^{+}(E_f) = P_s \tanh\left[\frac{E_f - E_c}{2\delta}\right], \tag{11}$$

for ascending E_f, and

$$P_{sat}^{-}(E_f) = -P_{sat}^{+}(-E_f), \tag{12}$$

for the descending branch, where P_s, E_c, and δ are the saturation polarization, coercive field, and idealized ferroelectric domain distribution parameter (δ being small or large for large or small domains representing domain interaction, respectively) (Appendix A). In order to use the above expressions for meaningful model calculations of experimental data, we implement numerical iteration schemes due to the nonlinear and hysteresis behavior of function $P_d(E_f)$. In particular, at given external potential V, $P_d(E_f)$ is expanded to first order in E_f, where the derivative is obtained analytically from differentiation of Eqs. (11) and (12) (Appendix A), and evaluated at given E_f. E_f, w_1, and w_2 are then calculated using Eqs. (4)–(6) in linear expansion for $P_d(E_f)$. Appendix C summarizes the linear expansions. The pivoting parameters for the selection of the calculation scheme in this iteration approach are w_1 and w_2. Depending on whether w_1 and w_2 are both or individually negative, zero, positive, or larger than d_{z1} and d_{z2}, respectively, the corresponding scheme of (A)–(I) is selected. For negative w_1 and/or w_2, the respective value(s) is (are) set to zero. Likewise, for w_1 and/or w_2 larger than d_{z1} and/or d_{z2}, the corresponding value(s) is (are) set to d_{z1} and/or d_{z2}, respectively. Calculation of E_f, P_d, w_1, and w_2 is repeated until convergence for all varied parameters is obtained. For calculations, reasonable but otherwise arbitrary initial parameter settings are used. Typically, after few iterations, E_f, P_d, w_1, and w_2 converge to a stable solution. As a result, the internal electric field variation within the structure is obtained, which allows for calculation of the heterostructure response within the ST circuit. Furthermore, the variation in P_d versus V_{in} is also obtained, which unravels the hysteresis functionality of layer F within the PFP heterostruc-

ture. This functionality will be discussed together with the ST response in Sec. IV.

III. EXPERIMENT

A. Sample preparation

The BTO and ZnO layers were deposited by PLD, successively without breaking the vacuum. The substrate temperature and the background pressure while growing these materials were 700 °C and 0.06 mbar, respectively. The number of laser pulses was 10^5 for BTO and 2×10^4 for ZnO. A pulse energy of 600 mJ was used. The BTO and ZnO layers were highly textured polycrystalline [BTO with (111) and ZnO with (0001) texture]. The metal electrodes were grown by sputtering Pt ohmic contacts. Structural, optical, and electrical analysis were performed as described previously.[12,54–59] The ZnO layers are *n*-type conductive, with free electron concentration N_c between $1\times10^{16}-1\times10^{17}$ cm^{-3}. Net donor densities were determined by electrical Hall effect and Infrared Ellipsometry characterization.[52] The BTO layer is highly resistive. Pt-BTO-Pt reference structures were prepared in the same PLD system.

B. Polarization measurements

All samples including the Pt-BTO-Pt reference structures were investigated by ST measurements (Appendix B) with varying amplitudes (V_{P-P}) of sinusoidal sweep voltage at frequency f. The electrical polarization of the structure was monitored with reference to a normal (hysteresis free) capacitor ($C_{st}=1$ μF). An external voltage V_{in} is applied in series to the sample and C_{st}. The potential variation V_o across C_{st} is monitored as a function of V_{in}. Hysteresis properties are measured by cyclic (time-harmonic) variations in V_{in}, which result in loop formation of V_o versus V_{in}.

IV. RESULTS AND DISCUSSIONS

A. Single-layer F: Model

With $d_{z1}=d_{z2}=0$ and $P_{sz1}=P_{sz2}=0$ the single-layer ferroelectric capacitor situation, i.e., a single ferroelectric layer sandwiched between ideal capacitor plates, is retained as solution within our model approach. Detailed discussions and presentations are omitted for brevity. A model comparison with experimental ST data from a single-layer BTO structure is discussed in Sec. IV D. Note that the internal ferroelectric domain configuration is approximated here as a quasisingle domain with effective ferroelectric polarization properties by means of Eqs. (A1)–(A4).

B. Double-layer PF: Model

The double-layer situation is obtained by setting $P_{sz1}=P_{sz}$, $P_{sz2}=0$, and allowing for schemes (A), (B), and (E) only. Figure 2 depicts calculated loops V_o versus V_{in}, and P_d versus V_{in} for different values of P_{sz}. Parameters used for calculation are summarized in Table II. In particular, the graphs in Fig. 2 depict the influence (existence and direction)

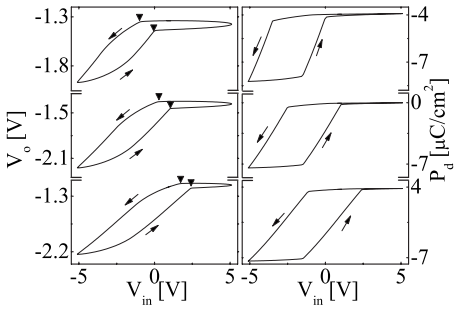

FIG. 2. Model calculated ST (left panel) and corresponding P_d traces versus V_{in} (right panel) for different values of P_{sz} (traces top to bottom: −4, 0, 4 μC m^{-2}) for a double-layer PF structure. Arrows indicate the sweep direction ($V_{P-P}=5$ V, $f=1.5$ kHz). Solid triangles indicate transitions between schemes (A) ($w=0$) and (B) ($d_z>w>0$). Model parameters are listed in Table II.

of spontaneous polarization P_{sz} of layer P onto the electrical properties of the double-layer PF heterostructure. The heterostructure reveals a diodelike behavior. For negative bias V_{in} the structure renders the forwardlike ("F" in Table I) bias characteristics of a semiconductor junction diode. Layer P is conductive, and the overall capacitance of the structure is

TABLE II. Best-match model calculation parameters for right and left layers P in Fig. 1 (thickness $d_{z1}=d_{z2}=d_z$, spontaneous polarization P_{sz}, net donor densities N_{c1}, N_{c2}, and dielectric constant ε_z), layer F (thickness d_f, remanent polarization P_r, saturation polarization P_s, coercive field E_c, and dielectric constant ε_f), conduction-band offset V_{bi} between P and F, ST parameters for normal capacitor C_{st}, normal capacitor resistance R_n, ST frequency f, and sample series resistance R_s. All varied parameters are found with 1% uncertainty with standard (90%) confidence interval.

	Best-match model values		
Parameter	BTO	BTO-ZnO	ZnO-BTO-ZnO
$d_{z1}=d_{z2}$ (μm)	0	0.5	0.5
d_f (μm)	1.5	1.45	1.4
N_{c1} (10^{17} cm^{-3})		0.55	2.9
N_{c2} (10^{17} cm^{-3})			2
V_{bi} (V)	0	-0.78 ± 0.2	0
ε_f	202	250	80
ε_z		8	6
R_n (MΩ) [a]	1	1	1
C_n (μC) [b]	1	1	1
E_c (MV/m)	1.15	1.1	1.1[c]
P_s (μC cm^{-2})	7.54	14.1	6
P_r (μC cm^{-2})	1.39	5.6	0.11
f (kHz)[d]	1.5	1.5	1.5
R_s (kΩ)	1000	13	1000
P_{sz} (μC cm^{-2})		−4.1	−0.1

[a]Parameter from measurement, not varied.
[b]Parameter from measurement, not varied.
[c]$E_c=1.1$ MV/m($V_{P-P}=12$ V); $E_c=0.957$ MV/m($V_{P-P}=10$ V); $E_c=0.781$ MV/m($V_{P-P}=8$ V); $E_c=0.622$ MV/m($V_{P-P}=6$ V).
[d]Parameter from measurement, not varied.

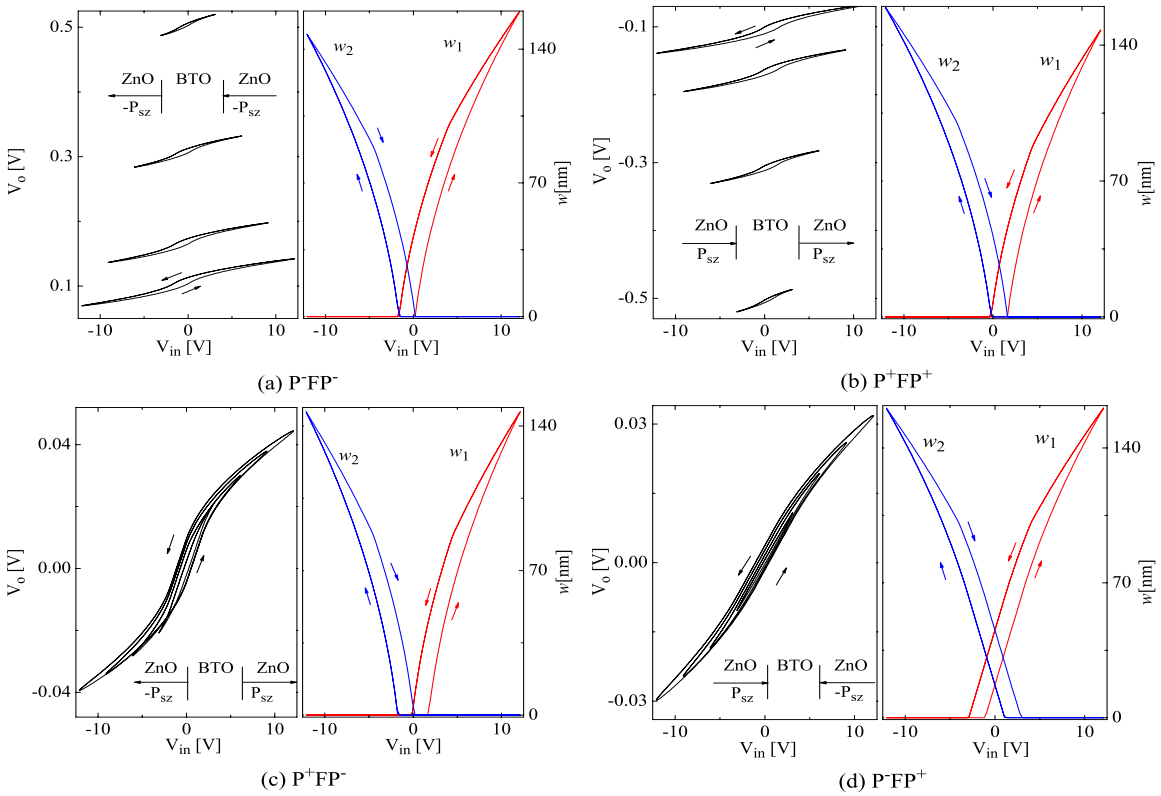

FIG. 3. (Color online) Model calculated ST data [left panels in Figs. 3(a)–3(d); sweeping voltages $V_{P-P}=3$, 6, 9, 12 V, $f=1.5$ kHz] and w_1, w_2 [right panels in Figs. 3(a)–3(d); $V_{P-P}=12$ V only] for triple-layer PFP heterostructure, and four different piezoelectric polarization vector orientations. Note that (a) and (b) correspond to simple contact reversal in Fig. 1, whereas (c) and (d) render two different physical structures. Arrows indicate voltage sweeping direction. Model parameters are those summarized in Table II for a ZnO-BTO-ZnO heterostructure, discussed in Sec. IV F.

established by layer F only. For positive external voltage, however, free electrons are gradually withdrawn from layer P, forming a depletion layer $w>0$ with reverselike ("R" in Table I) bias characteristics thereby adding a small series capacitance to the overall sample. Hence, the slope of V_o versus V_{in} decreases considerably since most of V_{in} now drops across the sample, and not across the test capacitor. Within a series of capacitances, the overall capacitance is dominated by the small capacitance due to layer w. Thus the potential across layer F is small and E_f remains small, reflected by the nearly constant P_d (right panel of Fig. 2). In "forward" direction ($w=0$), the electric field drops almost completely across the BTO layer and the ferroelectric polarization follows its typical hysteresis. In "reverse" direction, the ferroelectric polarization remains mostly within the negative part of the hysteresis loop. P_{sz} shifts the transition at which depletion layer formation occurs, i.e., the threshold between "reverse" and "forward" direction. The onset of the depletion layer formation and the associated capacitance change is shifted to negative ($P_{sz}<0$) or positive voltages ($P_{sz}>0$). The transitions where the depletion layer switches between zero and nonzero are indicated by vertical solid triangles in the left panel of Fig. 2. Note that in "reverse" direction, P_d approaches P_{sz}. Due to the nonlinear functionality and hysteresis of P_d versus E_f, the influence of P_{sz} is nonlinear as well, and the numerical value of P_{sz} can be not directly read from the ST data. Therefore, a best-match model calculation must be performed for analysis of the experimental data.

C. Triple-layer PFP: Model

The triple-layer PFP heterostructure renders a layered unipolar ferroelectric Bi-junction transistor with open base contact or double-diode arrangement, with common electrode anode and/or cathode combination depending on the external bias and combination of P_{sz1} and P_{sz2}. As discussed below, the physical mechanisms within the polarization-coupled interfaces for the different schemes allow for interesting device applications. Figure 3 depicts model calculated ST data together with w_1, w_2 for a hypothetical ZnO-BTO-ZnO heterostructure for the four polarization vector arrangements. Model parameters are those in Table II, except for $P_{sz}=0.2$ $\mu C/cm^2$. Note that for the calculations in Fig. 3 we assumed $N_{c1}=N_{c2}=2\times10^{17}$ cm^{-3}. The ST loops are shown for different sweeping voltages, and w_1, w_2 are shown for $V_{P-P}=12$ V only. Panels in Figs. 3(a)–3(d) correspond to arrangements P^-FP^-, P^+FP^+, P^-FP^+, and P^+FP^-, respectively.

Arrangements P^-FP^- and P^+FP^+ result in equivalent data as expected, which follow from simple physical contact inversion (voltage axis and abscissa inversion). For arrangements P^-FP^- and P^+FP^+ the heterostructure remains within schemes (B) and (C), i.e., either one of w_1 or w_2 is zero or finite, and both depletion layers are neither zero nor finite at

the same voltage. When the voltage sweeps from negative to positive, the heterostructure is represented by scheme (C), and w_1 is zero. When w_2 approaches zero, the heterostructure switches between operation schemes (C) to (B). For P^-FP^- (P^+FP^+) the symmetric P_{sz} orientations produce positive (negative) charge at the right and negative (positive) charge at the left interface of layer F (Fig. 1). The depletion layer widths for ground and biased layer P reach different values at maximum input voltage. As a result, the voltages at which the depletion layers disappear are not symmetric, and shift to negative (positive) values for P^-FP^- (P^+FP^+). This asymmetric depletion layer formation causes asymmetric charging upon cyclic external voltage variation, which is reflected by downward (upward) shift of the ST loop for P^-FP^- (P^+FP^+) with increasing V_{P-P}. In scheme (B) the heterostructure is composed of a series of diodes in "forward" (junction PF)–"reverse" (junction FP) condition, and in (C) it resembles a series of diodes in "reverse"-"forward" condition (Table I). Brief biasing by short voltage pulses can set the bijunction heterostructure into (i) sequence "reverse"-"forward" or (ii) "forward"-"reverse". For P^-FP^- (P^+FP^+), depending on the heterostructure parameters, a negative (positive) voltage region exists where both sequences (i) and (ii) can be found depending on P_d. The double-interface polarization coupling revealed in this heterostructure provides a switchable double-diode structure, where at nonzero bias a bistable configuration can be obtained exploiting the switchable polarization of layer F.

Arrangements P^-FP^+ and P^+FP^- result in ST data without loop shift and symmetric depletion layer formation. In addition to schemes (B) and (C), scheme (A) [sequence (iii) "forward"-"forward"] and (D) [sequence (iv) "reverse"-"reverse"] occur. Operation in scheme (A) occurs for P^-FP^+ for descending V_{in} from approximately 0 V to −2 V (w_1 disappears at approximately 0 V and w_2 remains zero until approximately −2 V) and for ascending V_{in} from approximately 0 to 2 V. For P^+FP^- operation in scheme (D) for descending V_{in} from approximately 0.5 to −3 V (w_1 disappears at approximately −2.5 V and w_2 opens at approximately 0.5 V) and for ascending V_{in} from approximately −0.5 to 3 V, whereas scheme (A) does not occur. The asymmetric P_{sz} orientations produce symmetric negative charges at the right and left interface of layer F. As a result, the depletion layer widths for ground and biased layers P reach symmetric values for $V_{in}=\pm V_{P-P}$. This symmetric depletion layer formation causes symmetric capacitance values for positive and negative potential drops between the sample electrodes and thus results in a symmetric ST loop centered at zero output voltage. In principle, the bijunction device can be electrically switched between four possible diode-diode sequences. The choice of materials with properties P_{sz}, $P_d(P_s, P_r, E_c)$ determines the voltage regions in which these situations can be obtained. Similar to the double-layer FP situation, due to the nonlinear functionality and hysteresis of P_d versus E_f, the influence of P_{sz1}, P_{sz2} is nonlinear as well, and the numerical value and orientation of $P_{sz1,2}$ cannot be directly read from the ST data. Therefore, a best-match model calculation must be performed for analysis of experimental data.

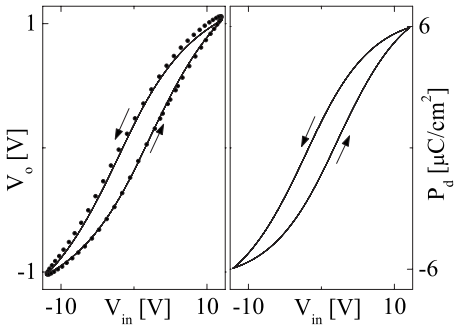

FIG. 4. Left panel: experimental (dotted line) and best-match model calculated ST data (solid line) from a single-layer F structure (Pt-BTO-Pt). Right panel: corresponding best-match model calculated ferroelectric polarization P_d within layer F (BTO). Best-match model parameters are given in Table II. Arrows indicate the input voltage sweep direction ($V_{P-P}=12$ V, $f=1.5$ kHz, $P_{sz1}=P_{sz2}=0$).

D. Single-layer F: Experiment

The left panel of Fig. 4 depicts experimental ST data and best-match model calculations for a single-layer F structure with ohmic metal contacts (Pt-BTO-Pt). The ST data reveal the typical ferroelectric hysteresis behavior. Domain formation within the polycrystalline film causes broadening (softening) of the ferroelectric switching behavior. This structure trivially operates in scheme (A), and the applied external potential is responsible for changes in P_d and internal electric field E_f within in layer F. Note that $P_{sz1}=P_{sz2}=0$. The right panel of Fig. 4 graphs the best-match model calculated trace of P_d versus applied voltage. The shape of the polarization loop is similar to the ST loop since all capacitance changes within the single-layer F structure are only caused by P_d, the polarization of layer F, which is directly proportional to the inverse capacitance of layer F. Slight deviations from the model and experimental ST data at positive voltages indicate formation of small accumulation layers at the interface of the Pt-top contact, which are not further considered here as their influence is marginal. The best-match model calculations revealed remanent polarization P_r, saturation polarization P_s, coercive field E_c, and ε_f. d_f was obtained from structural analysis. All parameters are summarized in Table II. Parameters obtained for P_r, E_c, and ε_f are within the range of previously reported data.[68–70] The magnitude of P_s is about two to four times smaller than typical values reported from bulk single-crystal measurements. Smaller values are often observed in polycrystalline film samples, where full saturation may not be reached due to limitations in applicable voltages without irreversible formation of electrical breakthroughs.[71–74]

E. Double-layer PF: Experiment

Figure 5 depicts experimental and best-model calculated ST data together with the P_d variations in layer F for a double-layer PF structure and for different maximum sweeping voltages V_{P-P}. The best-match model parameters are given in Table II. Triangles indicate the transitions between schemes (A) and (B), indicative for depletion layer formation within the ZnO layer as predicted within our model scheme

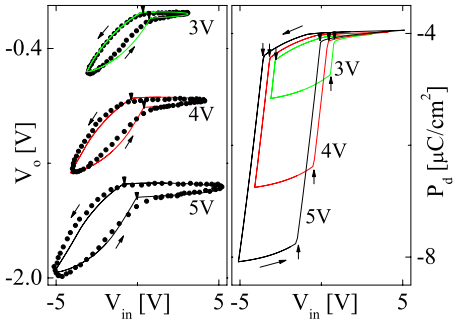

FIG. 5. (Color online) Same as Fig. 4 for the double-layer PF heterostructure (Pt-ZnO-BTO-Pt; $V_{P-P}=3$, 4, and 5 V; $f=1.5$ kHz; $P_{sz}=-4.1$ $\mu C/cm^2$).

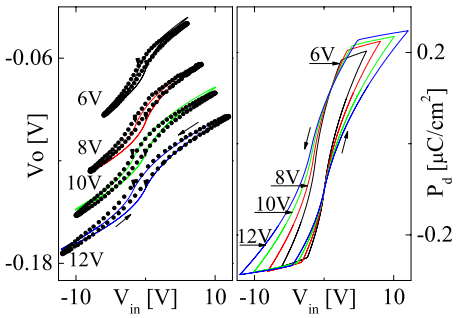

FIG. 6. (Color online) Same as Fig. 4 for the triple-layer PFP heterostructure (Pt-ZnO-BTO-ZnO-Pt; $V_{P-P}=6$, 8, 10, and 12 V; $f=1.5$ kHz).

developed in Sec. II. Note that for this experiment full depletion condition, i.e., scheme (E), is not reached. The ST data reflect the diodelike behavior of the overall heterostructure. The experimental data proof our suggested concept of interface polarization coupling. Both ZnO and BTO spontaneous polarizations determine the voltages of the transition points (triangles), which shift along the abscissa for increasing V_{P-P}. The separation between the transition points for "reverse" and "forward" directions are influenced by the ferroelectric hysteresis of the BTO layer. The separation is sensitive to model parameters E_c, P_s, and P_r for layer F. The right panel in Fig. 5 indicates ferroelectric polarization (downward arrows) and depolarization (upward arrows). On the ascending traces in Fig. 5, magnitude and orientation of P_{sz} are responsible for the voltage separation between transition (A)-(B) (right triangle on each loop, left panel) and depolarization transition (upward arrows, right panel). Transition (A)-(B) occurs prior to depolarization, thus P_{sz} must be negative. For $P_{sz}=0$ both transitions would occur at the same input voltage. From our best-match model calculation we derive the spontaneous polarization of ZnO as $P_{sz}=-4.1$ $\mu C\ cm^{-2}$. This value matches very well with previous literature values 7 ± 2 $\mu C\ cm^{-2}$.[24,30,31,75] The BTO coercive field ($E_c=11$ kV/cm) corresponds well to within typical values (1.5 to 50 kV/cm) for BTO thin layers reported previously.[68–70] Parameter N_c is in agreement with electrical Hall and infrared ellipsometry measurements.[52] Due to the diodelike behavior of the heterostructure, different charge accumulation occurs at positive and negative bias. The center of gravity of the polarization loop remains negative. In "reverse" configuration smaller charge accumulation occurs and subsequently smaller ferroelectric polarization than in "forward" situation. Accordingly, the best-match calculated traces P_d reveal large negative polarization in scheme (A) and almost zero polarization in scheme (B), as discussed in Sec. IV B. For larger V_{P-P}, P_d in "forward" situation increases, causing further negative charging (downward shift of ST data), which is quantitatively described by our model approach. A similar voltage-dependent polarization drift was observed previously in MFS heterostructures and was qualitatively explained with asymmetric leakage currents.[7–11]

F. Triple-layer PFP: Experiment

Figure 6 depicts experimental and best-model calculated ST data together with the P_d variations in layer F for a triple-layer PFP situation at various V_{P-P}. Similar to the double-layer structure, best-model calculated and experimental data are in very good quantitative agreement. The best-match model parameters are summarized in Table II. From the analysis procedure we identify transitions between schemes (B) and (C) (triangles, left panel) where our sample switches between (i) sequence "reverse"-"forward" (on descending side of loop) and (ii) "forward"-"reverse" (on ascending side of loop). Note that the switching voltages are not symmetric with respect to zero bias, and are shifted to negative bias. Comparison with Fig. 3 identifies that our structure belongs to configuration P^-FP^-, i.e., both ZnO layers posses negatively oriented (toward the substrate) spontaneous polarization vector orientations. Note that calculations in Fig. 3 ideally assumed equivalent net donor concentration in both layers P, whereas best-model calculations revealed slightly different concentrations within the ZnO layers (Table II; N_{c1} and N_{c2} are found in agreement with electrical Hall and infrared ellipsometry measurements).[52] Because $N_{c1}>N_{c2}$, further asymmetric charge accumulation occurs, which causes an overall downward shift of the experimental ST data with respect to those in Fig. 3(a). From our best-match model analysis we identify a much smaller value of $P_{sz}=-0.1$ $\mu C\ cm^{-2}$ for this heterostructure than for the double-layer structure discussed above. The latter finding may be explained by domain formation within the ZnO layers, in which neighboring domains may possess alternating polarization vector orientations. The heterostructure response is then affected by the average over multiple domain orientations.

As discussed in Sec. IV C, the triple-layer PFP heterostructure renders a unipolar bijunction transistor device, in which two diodes are connected in series. Note that this bijunction configuration does not require electrical contact to the base region and establishes a simple two-terminal device. Depending on P_d, at certain voltages, the two diodes can be set into bistable situations. Brief biasing by short voltage pulses here switch the bijunction heterostructure into situations (i) or (ii) and in which the heterostructure static series resistance is slightly different, e.g., at a given "read" voltage of 1 V. Bistable switching operation of this heterostructure was presented recently.[59] A similar switching behavior was observed previously in metal-ferroelectric-metal heterostructures and explained by the occurrence of serial diode arrangements. Bouregba *et al.* demonstrated upon a single-

layer dielectric continuum model calculations augmented by parallel circuits of diode-resistance pairs that such hysteresis offset can occur due to asymmetric resistance changes. In their series model, two pairs of antiparallel oriented diodes with two different resistances mimic the effect of different leakage currents within the ferroelectric layer over the metal interface barriers into the metal contacts.[11] In our heterostructures, the diodelike behavior originates from the variation in the depletion layers and the ferroelectric polarization.[59] The PFP heterostructures discussed in our work possess potential for new ferroelectric-semiconductor thin-film device applications.

V. CONCLUSIONS

We have presented and applied a model to explain and quantify the polarization response of interface polarization coupled piezoelectric-semiconductor ferroelectric heterostructures. Our model approach consist of the augmentation of depletion layer formation within a series layer capacitance calculation, which predicts the occurrence of asymmetric charging and polarization properties caused by the coupling between the switchable and nonswitchable polarization. Experimental investigations performed on single-layer BTO, double-layer ZnO-BTO, and triple-layer ZnO-BTO-ZnO heterostructures are in very good agreement with our theoretical model approach. Our model approach allows for the derivation of the magnitude and orientation of the spontaneous polarization of the piezoelectric constituent from experiment. We identify interface polarization coupled triple-layer ZnO-BTO-ZnO heterostructures as two-terminal unipolar ferroelectric bijunction transistor for possible application in memory storage.

ACKNOWLEDGMENTS

We acknowledge support by the Deutsche Forschungsgemeinschaft within the Sonderforschunsgbereich SFB 762 "Functional Oxide Interfaces," the CoE at UNL, the J. A. Woollam Foundation, NSF-DMR MRSEC QSPIN Grant No. 0820521, NSF-DMR Grant No. 0907475, and NSF-DMR Grant No. 0922937.

APPENDIX A: HYPERBOLIC TANGENT FUNCTION FERROELECTRIC POLARIZATION MODEL

An electric field-dependent ferroelectric polarization model can be obtained from the following phenomenological equations:[2]

$$P_{\mathrm{sat}}^{+}(E_{\mathrm{f}}) = P_{\mathrm{s}} \tanh\left[\frac{E_{\mathrm{f}} - E_{\mathrm{c}}}{2\delta}\right], \tag{A1}$$

where the plus sign in the superscript indicates the dipole saturation polarization P_{sat}^{+} on the lower branch of the saturated polarization hysteresis loop at electric field E_{f} after a given electric field increment. E_{c} denotes the coercive field. The quantity δ is obtained from

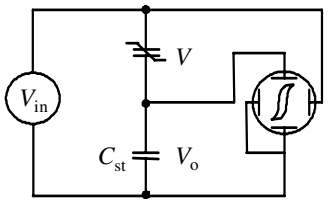

FIG. 7. Sawyer-Tower circuit.

$$\delta = E_{\mathrm{c}}\left[\log\left(\frac{1 + P_{\mathrm{r}}'/P_{\mathrm{s}}}{1 - P_{\mathrm{r}}'/P_{\mathrm{s}}}\right)\right]^{-1}, \tag{A2}$$

where P_{r}' denotes the remanent polarization and P_{s} is the maximum saturation polarization. P_{sat}^{-} after a given electric field decrement is obtained from Eq. (A1) as follows:

$$P_{\mathrm{sat}}^{-}(E_{\mathrm{f}}) = -P_{\mathrm{sat}}^{+}(-E_{\mathrm{f}}). \tag{A3}$$

For an unsaturated polarization formation P_{d} does not necessarily follow the saturation hysteresis loop. In order to calculate an unsaturated hysteresis loop we used the approach suggested by Miller.[3] In this model, the saturated and unsaturated polarizations at a given field E_{f} can be related by a factor Γ, which ensures smooth and monotonic approaching of the unsaturated polarization to the saturation polarization loop. This factor relates the first partial derivatives of both loops

$$\frac{\partial P_{\mathrm{d}}}{\partial E_{\mathrm{f}}} = \Gamma \frac{\partial P_{\mathrm{sat}}}{\partial E_{\mathrm{f}}} \tag{A4}$$

and

$$\Gamma = 1 - \tanh\left[\left(\frac{P_{\mathrm{d}} - P_{\mathrm{sat}}}{\xi P_{\mathrm{s}} - P_{\mathrm{d}}}\right)\right]. \tag{A5}$$

The factors $\xi=+1$ and $\xi=-1$ are for incrementing and decrementing fields E_{f}, respectively, and P_{d} is the (ferroelectric) dipole polarization on the unsaturated hysteresis loop at E_{f}, and P_{d} approaches P_{sat} for saturated polarization.

APPENDIX B: SAWYER-TOWER CIRCUIT MODEL

Figure 7 shows the schematic of the Sawyer-Tower circuit. C_{st} is a normal (standard) test capacitor, and V is the potential across a sample. V_{in} denotes the potential applied to the series of both capacitances. V_{o} is the output voltage measured across the normal capacitor. V_{bi} is the effective built-in potential (sum of all conduction band offsets) across the sample. The time derivative of the charge within the circuitry is described following Miller *et al.*;[2]

$$\frac{d}{dt}(-\sigma_{\mathrm{b}} A_{\mathrm{f}} + C_{\mathrm{st}} V_{\mathrm{o}}) = \frac{V_{\mathrm{in}} - V_{\mathrm{o}} - V_{\mathrm{bi}}}{R_{\mathrm{s}}} - \frac{V_{\mathrm{o}}}{R_{\mathrm{n}}}, \tag{B1}$$

where A_{f} is the contact area of the sample, R_{s} is the total (series) sample resistance between ground and bias electrode, and R_{n} is the normal capacitor resistance. With Eqs. (9) and (10), a differential relation is obtained for the PFP structure, which maps characteristic sample properties through experimental variation in V_{in} and measurement of V_{o}:

TABLE III. $w_{1_l}=(-b\pm\sqrt{b^2-4ac})/(2a)>0$, after iteration step $(l-1)$.

Scheme	a	b	c
(B)	$eN_{c1}/(2\varepsilon_z)$	$\dfrac{d_f eN_{c1}}{\varepsilon_f+\left(\dfrac{\partial P_d}{\partial E_f}\right)_{l-1}}$	$d_f\dfrac{P_{sz1}-P_{d_{l-1}}+\left(\dfrac{\partial P_d}{\partial E_f}\right)_{l-1}E_{f_{l-1}}}{\varepsilon_f+\left(\dfrac{\partial P_d}{\partial E_f}\right)_{l-1}}-V_l$
(D)	$(N_{c1}^2-N_{c2}^2)/N_{c1}$	$\dfrac{2(P_{sz2}-P_{sz1})}{eN_{c2}}N_{c1}+\dfrac{2\varepsilon_z d_f N_{c1}}{\varepsilon_f\left(\dfrac{\partial P_d}{\partial E_f}\right)_{l-1}}$	$-\dfrac{(P_{sz2}-P_{sz1})^2}{e^2N_{c2}}+\dfrac{2\varepsilon_z}{e}\left(V_l-d_f\dfrac{P_{sz1}-P_{d_{l-1}}+\left(\dfrac{\partial P_d}{\partial E_f}\right)_{l-1}E_{f_{l-1}}}{\varepsilon_f+\left(\dfrac{\partial P_d}{\partial E_f}\right)_{l-1}}\right)$

$$\frac{dV_o}{dt}=\frac{\dfrac{V_{in}-V_o-V_{bi}}{R_s}-\dfrac{V_o}{R_n}+\gamma\left(\varepsilon_f+\dfrac{dP_d}{dE_f}\right)A_f\dfrac{dV_{in}}{dt}}{C_{st}+\gamma\left(\varepsilon_f+\dfrac{dP_d}{dE_f}\right)A_f}. \quad \text{(B2)}$$

ST data represent the ratio of the inverse standard capacitance C_{st}^{-1} versus the sum of sample C_s^{-1} and standard C_{st}^{-1} inverse capacitances. The slope of the ST data is bound between 1 ($C_s\to 0$) and 0 ($C_s\to\infty$). For ideally nonconductive sample structures, a differential increase or decrease in the ST data slope at a given input voltage represents a decrease or increase in the sample capacitance, respectively.

APPENDIX C: ITERATION ALGORITHM

Equation (B2) is solved by iteration, which is adopted from Miller *et al.*[2] In this algorithm, external voltage loops are iterated, and at each voltage P_d, E_f, w_1, and w_2 are searched for iteratively, until convergence is obtained due to the nonlinear dependence between P_d and E_f. Convergence is reached when repeated loop calculations produce stable identical loops. At given external potential V_l, after $l-1$ iterations, P_{d_l} is calculated from

$$P_{d_l}=P_{d_{l-1}}+\left(\frac{\partial P_d}{\partial E_f}\right)_{l-1}(E_{f_l}-E_{f_{l-1}}). \quad \text{(C1)}$$

For calculation of E_f and subsequently $(\frac{\partial P_d}{\partial E_f})$, evaluation of w_{1_l}, w_{2_l} is necessary. From Tables III and IV one obtains solutions for w_{1_l} and w_{2_l}, respectively. The iterative scheme evaluates first w_{1_l}, w_{2_l}, according to scheme in step $l-1$, and polarization and electric field in step $l-1$. Inspection of w_{1_l}, w_{2_l} then determines if the current scheme (in step $l-1$) in Tables I, III, and IV is still valid in step l, or if it must be changed, i.e., if one and/or both depletion layers are zero, nonzero, or fully depleted. E_f is then calculated using the boundary conditions in Eqs. (5) and (6) for the appropriate scheme. No boundary exists in scheme (A), and we use Eq. (2)

$$E_{f_l}=\frac{V_l}{d_f}. \quad \text{(C2)}$$

Equation (5) or Eq. (6) is valid for schemes (B) and (E) or (C) and (F), respectively,

$$E_{f_l}=\frac{\pm eN_{c1,2}\omega_{1,2_l}+P_{sz1,2}-P_{d_l}+\left(\dfrac{\partial P_d}{\partial E_f}\right)_l E_{f_{l-1}}}{\varepsilon_f+\left(\dfrac{\partial P_d}{\partial E_f}\right)_l}, \quad \text{(C3)}$$

where the plus sign applies for (B) and (E), and the minus sign applies for (C) and (F). The sum of both boundary conditions is considered for the remaining schemes (D), (G), (H), and (I) in Table I

TABLE IV. $w_{2_l}=(-b\pm\sqrt{b^2-4ac})/(2a)>0$, after iteration step $(l-1)$.

Scheme	a	b	c
(C)	$eN_{c2}/(2\varepsilon_z)$	$\dfrac{d_f eN_{c2}}{\varepsilon_f+\left(\dfrac{\partial P_d}{\partial E_f}\right)_{l-1}}$	$V_l-d_f\dfrac{P_{sz2}-P_{d_{l-1}}+\left(\dfrac{\partial P_d}{\partial E_f}\right)_{l-1}E_{f_{l-1}}}{\varepsilon_f+\left(\dfrac{\partial P_d}{\partial E_f}\right)_{l-1}}$
(D)	$w_{2_l}=\dfrac{P_{sz2}-P_{sz1}-eN_{c1}w_1}{eN_{c2}}$		

$$E_{f_l} = \frac{\frac{1}{2}e[N_{c1}\omega_{1_l} - N_{c2}\omega_{2_l} + P_{sz1} + P_{sz2}] - P_{d_l} + \left(\frac{\partial P_d}{\partial E_f}\right)_l E_{f_{l-1}}}{\varepsilon_f + \left(\frac{\partial P_d}{\partial E_f}\right)_l}. \quad \text{(C4)}$$

Note that w_{1_l} in (B), (D), (G) and w_{2_l} in (C), (D), (H) are obtained as the physical meaningful (positive) branch of the quadratic equation following from Eq. (4), while $w_{1_l}=d_{z1}$ in (E), (H), (I) and $w_{2_l}=d_{z2}$ in (F), (G), (I).

[1] K. M. Rabe, C. H. Ahn, and J.-M. Triscone, *Physics of Ferroelectrics: A Modern Perspective* (Springer, New York, 2007).
[2] S. L. Miller, R. D. Nasby, J. R. Schwank, M. S. Rodgers, and P. V. Dressendorfer, J. Appl. Phys. **68**, 6463 (1990).
[3] S. L. Miller, J. R. Schwank, R. D. Nasby, and M. S. Rodgers, J. Appl. Phys. **70**, 2849 (1991).
[4] C. H. Tsang, C. K. Wong, and F. G. Shin, J. Appl. Phys. **98**, 084103 (2005).
[5] Z. Ye, M. H. Tang, C. P. Cheng, Y. C. Zhou, X. J. Zheng, and Z. S. Hu, J. Appl. Phys. **100**, 094101 (2006).
[6] A. N. Morozovska, E. A. Eliseev, D. Remiens, and C. Soyer, J. Appl. Phys. **100**, 014109 (2006).
[7] C. K. Wong and F. G. Shin, J. Appl. Phys. **98**, 024104 (2005).
[8] C. K. Wong and F. G. Shin, Appl. Phys. Lett. **86**, 042901 (2005).
[9] G. Poullain, R. Bouregba, B. Vilquin, G. L. Rhun, and H. Murray, Appl. Phys. Lett. **81**, 5015 (2002).
[10] L. Zheng, C. Lin, W.-P. Xu, and M. Okuyama, J. Appl. Phys. **79**, 8634 (1996).
[11] R. Bouregba, G. Poullain, B. Vilquin, and G. L. Rhun, J. Appl. Phys. **93**, 5583 (2003).
[12] M. Schubert, N. Ashkenov, T. Hofmann, M. Lorenz, H. Hochmuth, H. V. Wenckstern, M. Grundmann, and G. Wagner, Ann. Phys. **13**, 61 (2004).
[13] S.-Y. Wu, IEEE Trans. Electron Devices **21**, 499 (1974).
[14] M. Brandt, H. Frenzel, H. Hochmuth, M. Lorenz, M. Grundmann, and J. Schubert, J. Vac. Sci. Technol. B **27**, 1789 (2009).
[15] Y. Xu, C. J. Chen, R. Xu, and J. D. Mackenzie, J. Appl. Phys. **67**, 2985 (1990).
[16] L. S. Berman, Semiconductors **39**, 313 (2005).
[17] P. Wurfel and I. P. Batra, Phys. Rev. B **8**, 5126 (1973).
[18] P. Wurfel and I. P. Batra, Phys. Rev. B **10**, 1118 (1974).
[19] I. P. Batra, P. Wurfel, and B. D. Silverman, Phys. Rev. B **8**, 3257 (1973).
[20] L. S. Berman, Semiconductors **35**, 193 (2001).
[21] G. Z. Liu, K. J. Jin, J. Qiu, M. He, H. B. Lu, J. Xing, Y. L. Zhou, and G. Z. Yang, Appl. Phys. Lett. **91**, 252110 (2007).
[22] E. Cagin, D. Y. Chen, J. J. Siddiqui, and J. D. Phillips, J. Phys. D **40**, 2430 (2007).
[23] A. Malashevich and D. Vanderbilt, Phys. Rev. B **75**, 045106 (2007).
[24] A. Dal Corso, M. Posternak, R. Resta, and A. Baldereschi, Phys. Rev. B **50**, 10715 (1994).
[25] Y. Noel, C. M. Zicovich-Wilson, B. Civalleri, P. D'Arco, and R. Dovesi, Phys. Rev. B **65**, 014111 (2001).
[26] O. Ambacher *et al.*, J. Appl. Phys. **85**, 3222 (1999).
[27] O. Ambacher *et al.*, J. Appl. Phys. **87**, 334 (2000).
[28] M. Dawber, K. M. Rabe, and J. F. Scott, Rev. Mod. Phys. **77**, 1083 (2005).
[29] P. Gopal and N. Spaldin, J. Electron. Mater. **35**, 538 (2006).
[30] Y.-I. Kim, K. Page, and R. Seshadri, Appl. Phys. Lett. **90**, 101904 (2007).
[31] J. Jerphagnon and H. W. Newkirk, Appl. Phys. Lett. **18**, 245 (1971).
[32] S. Lautenschlaeger, J. Sann, N. Volbers, B. K. Meyer, A. Hoffmann, U. Haboeck, and M. R. Wagner, Phys. Rev. B **77**, 144108 (2008).
[33] M. W. Allen, S. M. Durbin, and J. B. Metson, Appl. Phys. Lett. **91**, 053512 (2007).
[34] M. W. Allen, P. Miller, R. J. Reeves, and S. M. Durbin, Appl. Phys. Lett. **90**, 062104 (2007).
[35] Y. Dong, Z.-Q. Fang, D. C. Look, G. Cantwell, J. Zhang, J. J. Song, and L. J. Brillson, Appl. Phys. Lett. **93**, 072111 (2008).
[36] R. Y. Gunji, M. Nakano, A. Tsukazaki, A. Ohtomo, T. Fukumura, and M. Kawasaki, Appl. Phys. Lett. **93**, 012104 (2008).
[37] D. Kohl, M. Henzler, and G. Heiland, Surf. Sci. **41**, 403 (1974).
[38] O. Dulub, U. Diebold, and G. Kresse, Phys. Rev. Lett. **90**, 016102 (2003).
[39] G. Heiland, P. Kunstmann, and H. Pfister, Z. Phys. A: Hadrons Nucl. **176**, 485 (1963).
[40] H. Tampo, P. Fons, A. Yamada, K.-K. Kim, H. Shibata, K. Matsubara, S. Niki, H. Yoshikawa, and H. Kanie, Appl. Phys. Lett. **87**, 141904 (2005).
[41] R. L. Barns, E. T. Keve, and S. C. Abrahams, J. Appl. Crystallogr. **3**, 27 (1970).
[42] A. N. Mariano and R. E. Hanneman, J. Appl. Phys. **34**, 384 (1963).
[43] S. Kazuta, Y. Cho, H. Odagawa, and M. Kadota, Jpn. J. Appl. Phys. **39**, 3121 (2000).
[44] M. Sambi, G. Granozzi, G. A. Rizzi, M. Casarin, and E. Tondello, Surf. Sci. **319**, 149 (1994).
[45] M. Galeotti, A. Atrei, U. Bardi, G. Rovida, M. Torrini, E. Zanazzi, A. Santucci, and A. Klimov, Chem. Phys. Lett. **222**, 349 (1994).
[46] T. Ohnishi, A. Ohtomo, I. Ohkuboa, M. Kawasaki, M. Yoshimoto, and H. Koinuma, Mater. Sci. Eng., B **56**, 256 (1998).
[47] S.-K. Hong, T. Hanada, H.-J. Ko, Y. Chen, T. Yao, D. Imai, K. Araki, and M. Shinohara, Appl. Phys. Lett. **77**, 3571 (2000).
[48] I. Ohkubo, A. Ohtomo, T. Ohnishi, Y. Mastumoto, H. Koinuma, and M. Kawasaki, Surf. Sci. **443**, L1043 (1999).
[49] M. Yano, K. Hashimoto, K. Fujimoto, K. Koike, S. Sasa, M. Inoue, Y. Uetsuji, T. Ohnishi, and K. Inaba, J. Cryst. Growth **301-302**, 353 (2007).
[50] A. Tsukazaki, A. Ohtomo, T. Kita, Y. Ohno, H. Ohno, and M. Kawasaki, Science **315**, 1388 (2007).
[51] H. Tampo *et al.*, Appl. Phys. Lett. **93**, 202104 (2008).

[52] C. Bundesmann, R. Schmidt-Grund, and M. Schubert, *Transparent Conductive Zinc Oxide*, Springer Series in Material Science, Vol. 104 (Springer, Berlin, 2007), Chap. Optical Properties of ZnO and Related Compounds.
[53] T. Bretagnon, P. Lefebvre, T. Guillet, T. Taliercio, B. Gil, and C. Morhain, Appl. Phys. Lett. **90**, 201912 (2007).
[54] B. N. Mbenkum, N. Ashkenov, M. Schubert, M. Lorenz, H. Hochmuth, D. Michel, M. Grundmann, and G. Wagner, Appl. Phys. Lett. **86**, 091904 (2005).
[55] V. M. Voora, T. Hofmann, M. Brandt, M. Lorenz, M. Grundmann, and M. Schubert, Phys. Status Solidi C **5**, 1328 (2008).
[56] N. Ashkenov, M. Schubert, E. Twerdowski, H. v. Wenckstern, B. Mbenkum, H. Hochmuth, M. Lorenz, W. Grill, and M. Grundmann, Thin Solid Films **486**, 153 (2005).
[57] V. M. Voora, T. Hofmann, M. Brandt, M. Lorenz, M. Grundmann, N. Ashkenov, and M. Schubert, J. Electron. Mater. **37**, 1029 (2008).
[58] V. M. Voora, T. Hofmann, M. Brandt, M. Lorenz, M. Grundmann, N. Ashkenov, and M. Schubert, Appl. Phys. Lett. **94**, 142904 (2009).
[59] V. M. Voora, T. Hofmann, M. Brandt, M. Lorenz, N. Ashkenov, M. Grundmann, and M. Schubert, Appl. Phys. Lett. **95**, 082902 (2009).
[60] V. M. Voora, T. Hofmann, M. Brandt, M. Lorenz, M. Grundmann, and M. Schubert, in *Theory and Applications of Ferroelectric and Multiferroic Materials*, edited by M. Dawber, MRS Symposia Proceedings No. 1110E (Material Research Society, Warrendale, PA, 2009), p. 1110-C06-14.
[61] A. L. Roytburd, S. Zhong, and S. P. Alpay, Appl. Phys. Lett. **87**, 092902 (2005).
[62] S. M. Nakhmanson, K. M. Rabe, and D. Vanderbilt, Appl. Phys. Lett. **87**, 102906 (2005).
[63] M. B. Okatan, M. W. Cole, and S. P. Alpay, J. Appl. Phys. **104**, 104107 (2008).
[64] A. M. Bratkovsky and A. P. Levanyuk, Phys. Rev. B **61**, 15042 (2000).
[65] M. B. Okatan, J. V. Mantese, and S. P. Alpay, Phys. Rev. B **79**, 174113 (2009).
[66] A. M. Bratkovsky and A. P. Levanyuk, Phys. Rev. Lett. **86**, 3642 (2001).
[67] E. D. Murray and D. Vanderbilt, Phys. Rev. B **79**, 100102(R) (2009).
[68] M. E. Line and A. M. Glass, *Principle and Applications of Ferroelectrics and Related Materials* (Clarendon, Oxford, 1977).
[69] A. Li, C. Ge, P. Lü, D. Wu, S. Xiong, and N. Ming, Appl. Phys. Lett. **70**, 1616 (1997).
[70] W. J. Lin, T. Y. Tseng, H. B. Lu, S. L. Tu, S. J. Yang, and I. N. Lin, J. Appl. Phys. **77**, 6466 (1995).
[71] B. A. Strukov, S. T. Davitadze, S. N. Kravchun, S. A. Taraskin, M. Goltzman, V. V. Lemanov, and S. G. Shulman, J. Phys.: Condens. Matter **15**, 4331 (2003).
[72] H. Miyazawa, E. Natori, T. Shimoda, H. Kishimoto, F. Ishii, and T. Oguchi, Jpn. J. Appl. Phys. **40**, 5809 (2001).
[73] T. Mitsui, I. Tatsuzaki, and E. Nakamura, *An Introduction to the Physics of Ferroelectrics* (GBSP, Inc., New York, 1976).
[74] D. Fu, M. Itoh, and S. Y. Koshihara, J. Phys.: Condens. Matter **22**, 052204 (2010).
[75] F. Bernardini, V. Fiorentini, and D. Vanderbilt, Phys. Rev. B **56**, R10024 (1997).